

# Topology-Induced Phase Transitions in Spin-Orbit Photonics

Xiaohui Ling, Fuxin Guan, Xiaodong Cai, Shaojie Ma, He-Xiu Xu, Qiong He, Shiyi Xiao,\*  
and Lei Zhou\*

Spin-controlled vortex generation and spin-Hall effect, two distinct effects discovered in optics, have been extensively studied recently. However, while physical origins of two effects are both due to spin-orbit interactions, their inherent connections remain obscure which also hinders further explorations on the manipulations of them. Here, in studying the scattering of a spin-polarized light beam at sharp interfaces, an intriguing phase transition between vortex generation and spin-Hall shift triggered by varying the incidence angle is revealed. After reflection/refraction, the beam contains two components: normal and abnormal modes acquiring spin-redirected-Berry phases and Pancharatnam–Berry phases, respectively. Inside the abnormal beam, two classes of wave components gain Pancharatnam–Berry phases with distinct topological natures, generating intrinsic and extrinsic orbital angular momenta (OAM), respectively. Enlarging incidence angle changes the relative portions of these two contributions, making the abnormal beam undergo a phase transition from vortex generation to spin-Hall shift. Such intriguing effect is experimentally observed at a purposely designed metamaterial slab, exhibiting efficiency enhanced by several-thousand times compared to that at a conventional slab. These findings unify two previously discovered effects in a single framework, reinterpret previous results with clearer pictures, and shed light on understanding other physical effects involving the competition between intrinsic and extrinsic OAM.

of a light beam as a whole and the intrinsic OAM (IOAM) describing the wave motions inside a light beam.<sup>[4]</sup> Such increased degree of freedom has generated more fascinating effects in light waves than those discovered on electrons.<sup>[5]</sup> For example, a conversion from SAM to EOAM takes place as a light beam propagates along a slowly varying path, resulting in photonic spin-Hall effect.<sup>[6–8]</sup> Meanwhile, a conversion from SAM to IOAM can happen as a circularly polarized light beam passes through a Q-plate made of inhomogeneous anisotropic medium, manifested by the generation of an optical vortex.<sup>[9–12]</sup> Such effect can never happen in rigid particles, but is solely determined by the wave nature of light, well explained by the Pancharatnam–Berry phase mechanism.<sup>[13,14]</sup>

Recently, these two distinct effects, previously discovered in different systems interpreted by different mechanisms, surprisingly appear in the same optical process. In 2004, Onoda et al.<sup>[15]</sup> predicted that, as a light beam with linear polarization (LP) strikes a sharp

interface, beams with different spins reflected/refracted from the interface can exhibit opposite spin-Hall shifts (**Figure 1**). Such effect was originally explained by a semi-classical theory<sup>[6–8]</sup> in analogy to the electron case, and soon re-examined by Bliokh et al.<sup>[16,17]</sup> who proposed a more accurate wave theory, which was quickly verified by Hosten et al. in experiments.<sup>[18,19]</sup> The physics is dictated by SOI arising as light changes its propagation

## 1. Introduction

Light possesses both spin angular momentum (SAM) and orbital angular momentum (OAM), and many spin-orbit-interaction (SOI)-induced effects were discovered recently.<sup>[1–3]</sup> Distinct from a rigid particle, light can exhibit two different types of OAMs, i.e., the extrinsic OAM (EOAM) describing the rotating motions

Prof. X. Ling, Dr. F. Guan, Dr. S. Ma, Prof. H.-X. Xu, Prof. Q. He,  
Prof. L. Zhou  
State Key Laboratory of Surface Physics  
Key Laboratory of Micro and Nano Photonic Structures (Ministry of  
Education) and Physics Department  
Fudan University  
Shanghai 200433, China  
E-mail: phzhou@fudan.edu.cn  
Prof. X. Ling  
College of Physics and Electronic Engineering  
Hengyang Normal University  
Hengyang 421002, China

Dr. X. Cai, Prof. S. Xiao  
Key laboratory of Specialty Fiber Optics and Optical Access Networks  
Joint International Research Laboratory of Specialty Fiber Optics and  
Advanced Communication  
Shanghai Institute for Advanced Communication and Data Science  
Shanghai University  
Shanghai 200444, China  
E-mail: phxiao@shu.edu.cn  
Prof. H.-X. Xu  
Air and Missile Defense College  
Air Force Engineering University  
Xi'an 710051, China  
Prof. Q. He, Prof. L. Zhou  
Collaborative Innovation Center of Advanced Microstructures  
Nanjing 210093, China

DOI: 10.1002/lpor.202000492

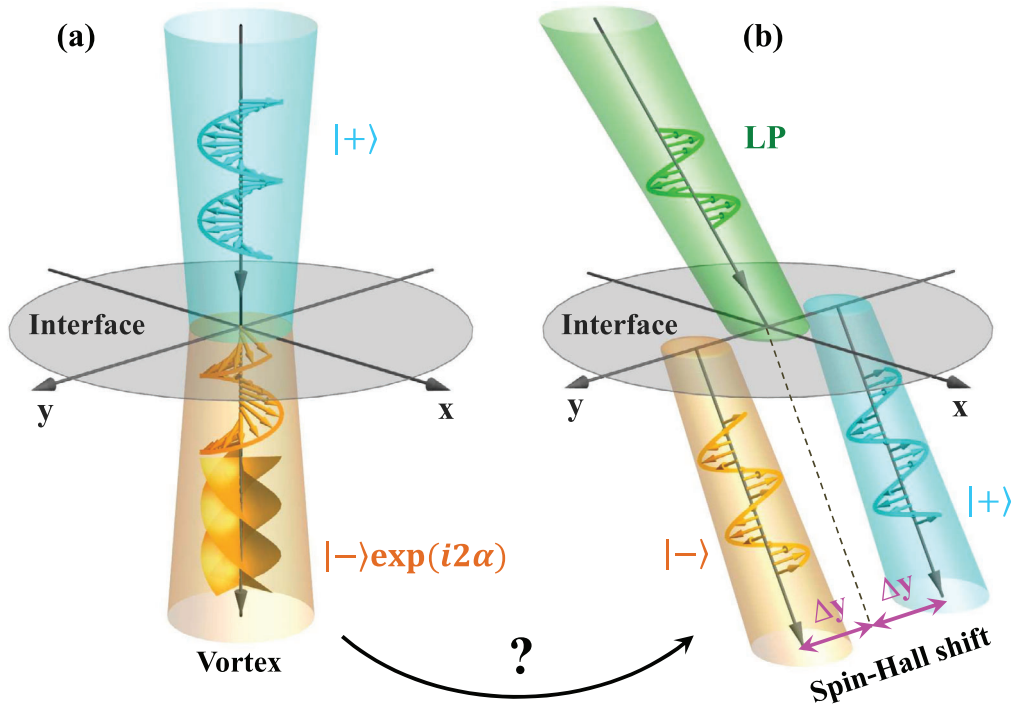


**Figure 1.** Two distinct effects happen as a light beam strikes an optical interface: a) an optical vortex is generated at normal incidence while b) the transmitted beams exhibit spin-Hall shifts ( $\pm\Delta y$ ) at large incidence angles.  $|\pm\rangle$ : CPs with different handedness; LP: linear polarization.

direction.<sup>[1,6–8]</sup> Obviously, such effect can only happen in oblique-incidence case where refraction can change the light propagation direction. On the other hand, some recent studies<sup>[20–22]</sup> showed that an optical vortex can be generated as a spin-polarized beam normally strikes an optical interface (Figure 1). Given two such distinct effects discovered in the same optical process, related to the conversion from SAM to OAM of different types, naturally one is curious to know the inherent connections between them and the way to control them in a desired manner.

In this work, we establish a unified theory to understand the two effects within a single framework, and uncover the physics governing their relations and intertransitions. We find that the light beam refracted by an optical interface contains a spin-maintained normal component and a spin-reversed abnormal one, with OAM properties dictated by the spin-redirection-Berry and Pancharatnam–Berry mechanisms, respectively. Wave components inside the abnormal beam can acquire Pancharatnam–Berry phases of different topological natures, which can generate either IAOM or EAOM, respectively. Varying the incidence angle can change the relative strengths of these two contributions, and thereby drive such SOI-induced effect transiting from the IAOM-related vortex generation to the EAOM-related spin-Hall shifts, passing through an intermediate regime where two effects co-exist. We finally design a realistic metamaterial slab and experimentally demonstrate such fascinating effect on such a slab with much enhanced efficiency (several thousand times larger than that of a slab made of conventional material). Our findings provide a unified explanation on diversified effects discovered in such a system, and can shed light on understanding many other SOI-related effects.

## 2. Theory and Results

### 2.1. Full-Wave Theory of Beam Scattering at Sharp Interfaces

We first establish a rigorous theory to study the scatterings of a light beam with circular polarization (CP) striking an air-dielectric interface at arbitrary angles (Figure 2a). We set the laboratory co-ordinate system as  $xyz$  and the local co-ordinate system as  $x^a y^a z^a$  with  $z^a$  parallel to the beam propagation direction. Here,  $y$  and  $y^a$  point to the same direction, and  $a = \{i, r, t\}$  label incidence, reflection, and transmission, respectively. In general, the incident/reflected/transmitted beams can be expanded as linear combination of plane waves

$$E^a(\mathbf{r}^a) = \int d^2\mathbf{k}_\perp^a e^{i\mathbf{k}_\perp^a \cdot \mathbf{r}_\perp^a} [u_+(\mathbf{k}^a)\hat{\mathbf{v}}_+(\mathbf{k}^a) + u_-(\mathbf{k}^a)\hat{\mathbf{v}}_-(\mathbf{k}^a)] \quad (1)$$

where  $\mathbf{k}^a \cdot \mathbf{r}^a = \mathbf{k}_\perp^a \cdot \mathbf{r}_\perp^a + k_z^a z^a$  with  $k_z^a = \sqrt{(k^a)^2 - (k_\perp^a)^2}$  and  $\mathbf{k}^a$  and  $\mathbf{r}^a$  denoting the wave vector and position vector in local coordinate system,  $\hat{\mathbf{v}}_\sigma(\mathbf{k}^a) = [\hat{\mathbf{v}}_{\text{TM}}(\mathbf{k}^a) + \sigma i\hat{\mathbf{v}}_{\text{TE}}(\mathbf{k}^a)]/\sqrt{2}$  ( $\sigma \in \{+, -\}$ ) denote unit vectors of left (+) and right (–) CPs with  $\hat{\mathbf{v}}_{\text{TE}}(\mathbf{k}^a) = \hat{\mathbf{z}} \times \mathbf{k}^a / |\hat{\mathbf{z}} \times \mathbf{k}^a|$  and  $\hat{\mathbf{v}}_{\text{TM}}(\mathbf{k}^a) = \hat{\mathbf{v}}_{\text{TE}}(\mathbf{k}^a) \times \mathbf{k}^a / k^a$  being the unit polarization vectors of transverse-electric (TE) and transverse-magnetic (TM) waves<sup>[23]</sup> defined in the laboratory co-ordinate system, and  $u_\pm^a(\mathbf{k})$  are the expansion coefficients. We use  $\theta_k^a$  to denote the directions of the central wave vector  $\mathbf{K}^a$  and  $\theta_k^a$  to denote the direction of an arbitrary plane wave (see Section S1, Supporting Information) inside the light beams (Figure 2b).

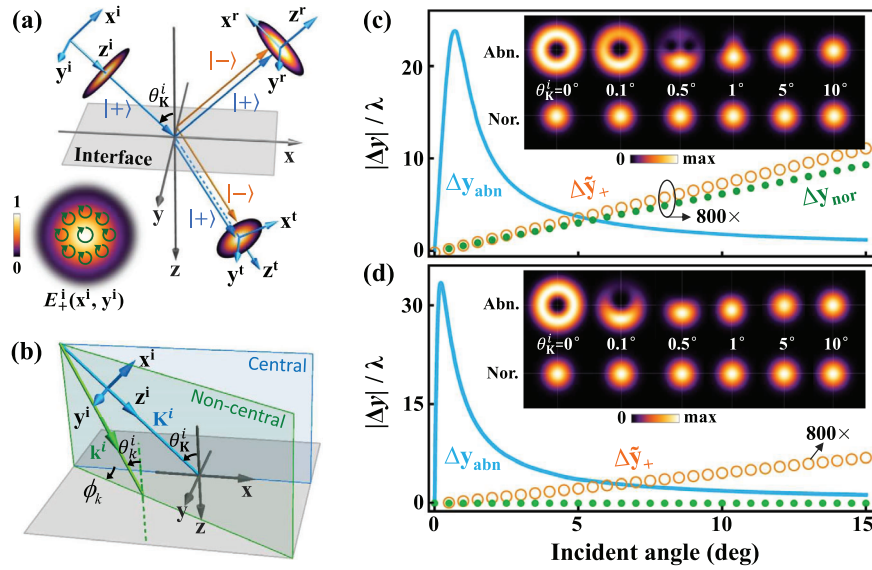


**Figure 2.** Spin-Hall shifts and evolution of intensity patterns. a) Scattering of a spin-polarized beam at an air/dielectric interface. Inset: E-field and polarization distribution of the incident beam on its waist plane ( $z^i = -10\lambda$ ). (b) Schematic of angles and incident planes of the central ( $K$ ) and noncentral plane waves ( $k$ ). Spin-Hall shifts of the normal/abnormal modes in the beams transmitted through c) a single interface and d) a thin dielectric slab.  $\Delta\tilde{y}_+$ : shifts calculated by previous theory. Insets: Transverse-field patterns of the abnormal/normal modes in the transmitted beams at a reference plane ( $z^t = 10\lambda$ ). Refractive index of the dielectric medium is set as 1.5, the slab's thickness  $h = 0.5\lambda$ , and  $w_0 = 55\lambda$ . 800  $\times$ : Data are magnified by 800 times.

For present scattering problem, we have

$$\begin{pmatrix} u_+^{r,t}(\mathbf{k}^{r,t}) \\ u_-^{r,t}(\mathbf{k}^{r,t}) \end{pmatrix} = \mathbf{F}^{(r,t)}(\mathbf{k}_\parallel) \begin{pmatrix} u_+^i(\mathbf{k}^i) \\ u_-^i(\mathbf{k}^i) \end{pmatrix} \quad (2)$$

to connect  $u_\pm^{r,t}(\mathbf{k}^{r,t})$  and  $u_\pm^i(\mathbf{k}^i)$  with  $\mathbf{k}^{r,t}$  and  $\mathbf{k}^i$  interconnected by Snell's law, where  $\mathbf{F}^{(r,t)}(\mathbf{k}_\parallel)$  are  $2 \times 2$  matrices with elements  $F_{\sigma\sigma'}^{(r,t)}(\mathbf{k}_\parallel)$  ( $\sigma' \in \{+, -\}$ ) being Fresnel's coefficients of waves with tangential wave vector  $\mathbf{k}_\parallel$  defined in the laboratory coordinate system.<sup>[23]</sup> To benefit further computations, we formally rewrite the E-field distributions on the reference planes ( $z^a = d^a$ ) as

$$\mathbf{E}_\pm^a(\mathbf{r}_\perp^a) = \int d^2\mathbf{k}^a e^{i\mathbf{k}^a \cdot \mathbf{r}_\perp^a} [U_+^a(\mathbf{k}^a)\hat{\mathbf{v}}_+(\mathbf{K}^a) + U_-^a(\mathbf{k}^a)\hat{\mathbf{v}}_-(\mathbf{K}^a)] \quad (3)$$

where all wave components are assumed to take the spin-vector of the central  $\mathbf{K}^a$ -vector. Here,  $U_\pm^a(\mathbf{k}^a)$  are related to  $u_\pm^a(\mathbf{k}^a)$  defined in Equation (1) via (see Section S2, Supporting Information for details)

$$\begin{pmatrix} U_+^a(\mathbf{k}^a) \\ U_-^a(\mathbf{k}^a) \end{pmatrix} = \mathbf{P}^{(a)} \begin{pmatrix} u_+^a(\mathbf{k}^a) \\ u_-^a(\mathbf{k}^a) \end{pmatrix} \quad (4)$$

where  $P_{\sigma\sigma'}^{(a)} = [\hat{\mathbf{v}}_\sigma(\mathbf{K}^a)]^* \cdot \hat{\mathbf{v}}_{\sigma'}(\mathbf{k}^a)$  are the elements of  $\mathbf{P}^{(a)}$ , representing a projection between spin-vectors of a wave with  $\mathbf{k}^a$  and the center one  $\mathbf{K}^a$ . Combining Equations (2) and (4), we finally obtain

$$\begin{pmatrix} U_+^{r,t}(\mathbf{k}^{r,t}) \\ U_-^{r,t}(\mathbf{k}^{r,t}) \end{pmatrix} = \mathbf{M}^{(r,t)} \begin{pmatrix} U_+^i(\mathbf{k}^i) \\ U_-^i(\mathbf{k}^i) \end{pmatrix} \quad (5)$$

where  $\mathbf{M}^{(r,t)} = \mathbf{P}^{(r,t)} \cdot \mathbf{F}^{(r,t)} \cdot (\mathbf{P}^{(i)})^{-1}$  (see Section S2, Supporting Information). Equation (5) is important, since it connects  $U_\pm^{r,t}(\mathbf{k}^{r,t})$

with  $U_\pm^i(\mathbf{k}^i)$ , which dictate the transverse patterns of the scattered and incident beams, respectively.

We assume that the incident beam is a Gaussian one with E-field on the waist-plane being

$$\mathbf{E}_\pm^i(\mathbf{r}_\perp^i) |_{z^i=d^i} = \exp[-(r_\perp^i/w_0)^2] \hat{\mathbf{v}}_\pm(\mathbf{K}^i) \quad (6)$$

where  $w_0$  is the beam width. Combining this equation with Equation (3), we get  $U_-^i(\mathbf{k}^i) \equiv 0$  and the expression of  $U_+^i(\mathbf{k}^i) = \frac{w_0^2}{2} \exp[-(k_\perp^i w_0)^2/4]$  via Fourier transforming the Gaussian term. Put  $U_\pm^i(\mathbf{k}^i)$  to Equation (5) to get  $U_\pm^{r,t}(\mathbf{k}^{r,t})$ , we finally obtain the E-field distributions on the reference planes of reflected/transmitted beams via putting  $U_\pm^{r,t}(\mathbf{k}^{r,t})$  into Equation (3).

## 2.2. Spin-Hall Shifts and Evolution of Intensity Patterns

Our theory can be used to describe the beam scatterings at arbitrary sharp interfaces with rotational invariance respect to  $z$ -direction, including single interfaces composed of two semi-infinite materials and the case of multi-layered media (e.g., an optical thin slab placed in air). We first employ the theory to rigorously study the intensity evolutions and spin-Hall shifts of transmitted beams as a single interface is illuminated at arbitrary incident angles  $\theta_K^i$ . Generally, matrix  $\mathbf{M}^{(r,t)}$  contains off-diagonal terms, so that the transmitted beam has two components, one with spin conserved ( $\sigma = +$ ) defined as the normal mode and the other with spin reversed ( $\sigma = -$ ) called the abnormal one. Inset to Figure 2c depicts the computed transverse field patterns of the normal/abnormal modes of the transmitted beam at different  $\theta_K^i$ . As  $\theta_K^i$  increases, while the normal mode always exhibits a well-defined Gaussian profile, the abnormal mode has very intriguing field-pattern evolutions showing a topological transition from vortex generation to spin-Hall shifts. Quantitatively, we

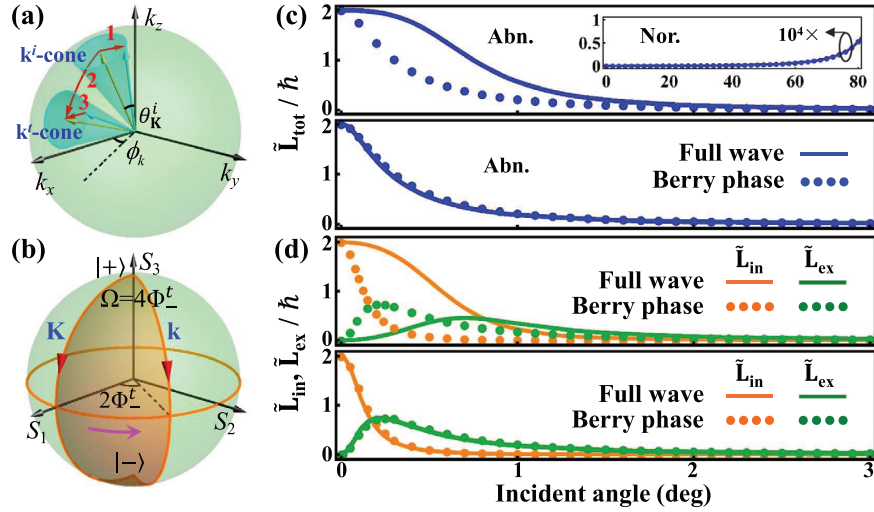


**Figure 3.** Two types of geometric phase and two OAMs. a) A spin-redirected-Berry phase is gained as a spin-polarized wave with  $\mathbf{k}'$  is refracted to that with  $\mathbf{k}^i$ , which is the integration of Berry curvature along the path 1-2-3. b) A PB phase is gained as a spin-up plane wave with  $\mathbf{k}$  undergoes a spin-reversed scattering, which is half of the solid angle  $\Omega$  of the shaded area enclosed by two paths connecting the north and south poles on the Poincaré sphere. c) Total OAM ( $\tilde{L}_{\text{tot}}$ ) of the abnormal mode in the beam transmitted through a single interface (upper) and a slab (lower), calculated by the full theory and Equation (9), respectively. Inset:  $\tilde{L}_{\text{tot}}$  of the normal mode with its value being magnified by  $10^4$  times. d)  $\tilde{L}_{\text{in,ex}}$  of the abnormal mode for single-interface (upper) and slab (lower) cases.

numerically evaluated the transverse shifts of beam centroids of two modes ( $\Delta y_{\text{nor}}$  and  $\Delta y_{\text{abn}}$ ) with the following formula

$$\Delta y = \frac{\iint y^a |E^a|^2 dx^a dy^a}{\iint |E^a|^2 dx^a dy^a} \quad (7)$$

and depict in Figure 2c how  $\Delta y_{\text{nor}}$  and  $\Delta y_{\text{abn}}$  vary against  $\theta_K^i$ . We find  $\Delta y_{\text{abn}}$  is nearly 1000 times larger than  $\Delta y_{\text{nor}}$ , and exhibits intriguing  $\theta_K^i$ -dependence compared to  $\Delta y_{\text{nor}}$ . Moreover, the  $\tilde{\Delta y}_+ \sim \theta_K^i$  curve calculated by previous theory<sup>[16–18]</sup> is very similar to the  $\Delta y_{\text{nor}} \sim \theta_K^i$  line obtained here.

We next repeat our calculations on an optically thin slab placed in air, and depict the corresponding results in Figure 2d. Compared to the single-interface case, here the normal and abnormal modes exhibit quite similar properties except that now  $\Delta y_{\text{nor}} \equiv 0$  is independent of  $\theta_K^i$ , in consistency with the computed patterns depicted in the inset. Intriguingly, the  $\tilde{\Delta y}_+ \sim \theta_K^i$  curve calculated by previous theory<sup>[16–18]</sup> is completely different from the two curves calculated by our theory, even with opposite evolution trend.

### 3. Underlying Physics of the Topology-Induced Phase Transitions

#### 3.1. Beam Deflection and Spin Reversal: Two Types of Berry Phase

We now simplify the full-wave theory based on the Berry phase concept.<sup>[24,25]</sup> Under the paraxial-wave approximation, we find the projection matrix  $\mathbf{P}^{(a)}$  is nearly diagonalized. Neglecting the off-diagonal elements, we get (see Section 3, Supporting Information)

$$\mathbf{P}^{(a)} \approx \begin{bmatrix} \exp(i\Phi_+^a) & \\ & \exp(i\Phi_-^a) \end{bmatrix} \quad (8)$$

where  $\Phi_+^a(\mathbf{k}^a) = -\Phi_-^a(\mathbf{k}^a)$  measures the phase difference between two CP unit-vectors associated with  $\mathbf{k}^a$  and  $\mathbf{K}^a$ , which is the Berry phase gained in the adiabatical process of a spin rotating from the direction of  $\mathbf{k}^a$  to  $\mathbf{K}^a$  (Figure 3a).<sup>[1,25]</sup> Putting  $\mathbf{P}^{(a)}$  into  $\mathbf{M}^{(t)}$ , we finally get

$$\begin{cases} E_{++}^t(\mathbf{r}_\perp^t) = \int d^2\mathbf{k}_\perp^t e^{i\mathbf{k}^t \cdot \mathbf{r}^t} t_{++}(\mathbf{k}_\parallel) e^{i\Phi_B^{\text{nor}}(\mathbf{k}^t)} U_+^i(\mathbf{k}^i) \\ E_{-+}^t(\mathbf{r}_\perp^t) = \int d^2\mathbf{k}_\perp^t e^{i\mathbf{k}^t \cdot \mathbf{r}^t} t_{-+}(\mathbf{k}_\parallel) e^{i\Phi_B^{\text{abn}}(\mathbf{k}^t)} U_+^i(\mathbf{k}^i) \end{cases} \quad (9)$$

to determine the fields of the normal and abnormal modes inside the transmitted beam. Here,  $t_{++}$  and  $t_{-+}$  are the spin-maintained and spin-reversed transmission coefficients, and

$$\Phi_B^{\text{nor}} = \Phi_+^t - \Phi_+^i, \quad \Phi_B^{\text{abn}} = \Phi_-^t - \Phi_+^i \quad (10)$$

are two Berry phases gained by a wave with  $\mathbf{k}^a$  inside the normal and abnormal modes, respectively. Careful analyses show that these two Berry phases have distinct origins. For the normal mode,  $\Phi_B^{\text{nor}}$  is a spin-redirected-Berry phase gained by the wave with  $\mathbf{k}^i$  undergoing the refraction process (i.e., the path 1-2-3 defined in Figure 3a), and can be rewritten as

$$\begin{aligned} \Phi_B^{\text{nor}}(\mathbf{k}^t) &= \int_{1-2-3} \mathbf{A}(\mathbf{k}) \cdot d\mathbf{k} \\ &= - \int_0^{\phi_k} A_{\phi_k}^i(\mathbf{k}^i) \sin \theta_k^i d\phi_k + 0 + \int_0^{\phi_k} A_{\phi_k}^t(\mathbf{k}^t) k^t \sin \theta_k^t d\phi_k, \\ &= -\sigma (\cos \theta_k^t - \cos \theta_k^i) \phi_k \end{aligned} \quad (11)$$

where  $\mathbf{A}^a(\mathbf{k}^a) = -i(\hat{\mathbf{v}}_\sigma^a)^* \cdot (\nabla_{\mathbf{k}})\hat{\mathbf{v}}_\sigma^a$  is the Berry connection with solely azimuthal component  $\mathbf{A}_{\phi_k}^a(\mathbf{k}^a) = -\sigma \frac{\cot \theta_k^a}{k^a} \hat{\mathbf{e}}_{\phi_k}$ .<sup>[1,24,25]</sup> Obviously,  $\Phi_B^{\text{nor}}$  is nonzero only as light changes its propagation direction, but disappears when  $\theta_k^i = \theta_k^t$  (e.g., normal incidence or the slab case) which explains why we have  $\Delta Y_{\text{nor}} \equiv 0$  in the slab case.

Meanwhile, rewriting  $\Phi_B^{\text{abn}}$  as

$$\Phi_B^{\text{abn}} = (\Phi_+^t - \Phi_+^i) + 2\Phi_-^t = \Phi_B^{\text{nor}} + 2\Phi_-^t \quad (12)$$

we find that  $\Phi_B^{\text{abn}}$  is dominated by  $2\Phi_-^t$  because of spin-reversal of the abnormal mode, which persists even without beam deflection. This term is a Pancharatnam–Berry phase,<sup>[1,9–14]</sup> representing the geometric phase gained by a spin associated with  $\mathbf{k}$  moving from the north (south) pole to the south (north) one on the Poincaré sphere along different paths (Figure 3b).

It is intriguing to see that, even for the simple case of light scatterings at a single interface, two different Berry phases co-exist and are collectively responsible for the physics governing the fascinating behaviors of the abnormal mode (see Figure 2c,d). In contrast, the physics of abnormal mode in the slab case is solely dictated by the Pancharatnam–Berry phase since the light does not change its propagation direction after passing through the slab.

### 3.2. Competition between intrinsic and Extrinsic Orbital Angular Momenta

We next use the simplified model [Equation (9)] to explore the underlying physics. Figure 3c compares the total OAMs ( $\tilde{L}_{\text{tot}}$ ) per photon in the  $z^t$ -direction calculated by the simplified and the full theory [Equations (9) and (3)] for two modes<sup>[3,4,26]</sup> (see Section S4, Supporting Information for detailed derivation), in both single-interface and slab cases. The simplified model has reproduced all salient features of the rigorous results. In particular, both formulas yield  $\tilde{L}_{\text{tot}} \equiv 0$  for the normal mode in the slab case, which are not shown here. While certain deviations exist between two theories in the abnormal mode for the single-interface case, caused by neglecting the off-diagonal terms in  $\mathbf{P}^{(i,t)}$ , the same is not true for the slab case where influences of these off-diagonal terms cancel each other because of  $\theta_k^t \equiv \theta_k^i$ .

We subsequently focus on the abnormal mode, which exhibits much more fascinating OAM properties than the normal mode. For the abnormal beam, the transverse field pattern at  $\theta_k^i = 0^\circ$  exhibits a donut shape, already implying the existence of IOAM, also consistent with the calculated value  $\tilde{L}_{\text{tot}} = 2\hbar$  (Figure 3c). This can also be obtained simply by considering the conservation of angular momentum in the laboratory  $z$ -direction, that is, the spin reversal changes the SAM of the abnormal mode from  $+\hbar$  to  $-\hbar$  per photon, which is converted into additional IOAM with  $+2\hbar$  per photon. To quantify the above arguments, we separately evaluated the IOAM ( $\tilde{L}_{\text{in}}$ ) and the EOAM ( $\tilde{L}_{\text{ex}}$ ) per photon<sup>[3,4,26]</sup> for the abnormal mode, and depict them as varying  $\theta_k^i$  in Figure 3d for two studied cases. Again, the Berry-phase formulas [Equation (9)] have grasped the key physics, yielding nearly identical results with the rigorous ones in the slab case. For both systems, we find the following common features: i) only IOAM exists and  $\tilde{L}_{\text{in}} = 2\hbar$  at  $\theta_k^i = 0^\circ$  implying the generation of an optical vortex;

ii) only EAOM exists at large  $\theta_k^i$ , consistent with the computed spin-Hall shifts shown in Figure 2; iii) as  $\theta_k^i$  increases, IOAM and EOAM compete with each other, eventually driving the system from an IOAM-dominated phase to EAOM-dominated one.

We note that two distinct SOI-induced effects (vortex-generation and spin-Hall effect) are now explained within a unified theoretical framework connected to the competition of IOAM and EOAM, while previously they are usually regarded as different effects and were separately considered.<sup>[15–18,20–22]</sup>

### 3.3. Topology-Induced Transition of the Pancharatnam–Berry Phase in Abnormal Mode

To explore the physics governing such a phase transition, we study the slab configuration which is very “clean” as  $\Phi_B^{\text{abn}} = 2\Phi_-^t$  only contains Pancharatnam–Berry phase. While  $\Phi_B^{\text{abn}}$  exhibits a complicated dependence on both  $\mathbf{k}^i$  and  $\mathbf{k}^t$ , we find that it shows a one-by-one correspondence with  $\phi_k$ , which is the azimuthal angle of  $\mathbf{k}^i$  in the laboratory system (Figure 4a). Under the paraxial-wave approximation and with small  $\theta_k^i$ , we get  $\Phi_B^{\text{abn}} \approx 2\phi_k$  (see Section S3, Supporting Information for details) which motivates us to directly examine the properties of  $\phi_k$ . Define the azimuthal and polar angles of  $\mathbf{k}^i$  in the local system as  $\alpha$  and  $\beta$  (Figure 4a) and consider the rotation between local and laboratory systems, we get  $\phi_k = \tan^{-1}(k_y/k_x)$  where (see Section 1, Supporting Information)

$$\begin{cases} k_x = k^i (\sin\beta \cos\alpha \cos\theta_k^i + \cos\beta \sin\theta_k^i) \\ k_y = k^i \sin\beta \sin\alpha \end{cases} \quad (13)$$

Figure 4b depicts how the quantity  $k_x + ik_y$  evolves as varying  $\alpha$  in the complex plane (i.e., the Smith curves) for  $\beta$  taking three typical values, each representing a specific cone of  $\mathbf{k}^i$  vectors inside the incident beam (Figure 4a). For the  $\mathbf{k}$ -cone with  $\beta/\theta_k^i = -1$ , we find a special solution  $k_x = k_y = 0$  of Equation (13) in the case of  $\alpha = 0^\circ$ , corresponding to the normally incident plane wave in the laboratory system. Interestingly, such a singular point (SP) separates all  $\mathbf{k}$ -cones into two distinct classes, with Smith curves enclosing or *not* enclosing the origin (Figure 4b), thus generating Pancharatnam–Berry phases covering the full  $4\pi$  range or only a small range, respectively. Such a physical picture is verified by our directly computed  $\Phi_B^{\text{abn}}$  distributions (Figure 4c), where the phase boundary (dotted lines) separating two classes of  $\mathbf{k}$ -cones (regions I and II) vary against  $\theta_k^i$ , as expected. In the lowest-order approximation, we can approximate  $\Phi_B^{\text{abn}}$  by  $2\alpha$  (vortex phase) in region I and  $2k_y^i \cot \theta_k^i / k^i$  ( $k_y^i$ -dependent gradient phase) in region II (inset to Figure 4d), which can be directly obtained by calculating Equation (10) and Equation (S3.3) in Section S3 of the Supporting Information. Clearly,  $\Phi_B^{\text{abn}}$  consists of two parts with distinct topological properties: one is the vortex phase with a phase singularity which contributes to the IOAM, while another is the gradient phase without phase singularity which contributes to the EOAM. Using such an approximate form of  $\Phi_B^{\text{abn}}$  to calculate IOAM and EOAM of the abnormal beam, we find that the obtained results (dotted lines in Figure 4d) are in reasonable agreement with the rigorous calculations (solid lines). The physics is thus clear:  $\mathbf{k}$ -cones exhibiting distinct topologies can generate either IOAM or

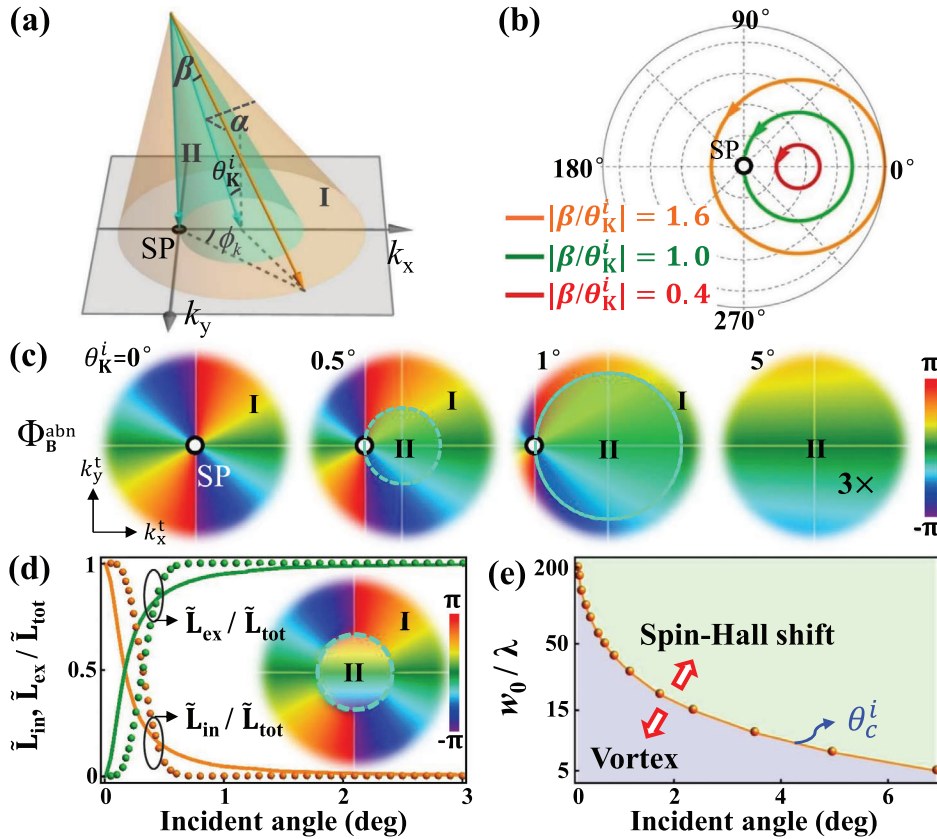


**Figure 4.** The mechanism of topology-induced phase transitions. a) Fourier-representation of the incident beam containing two nested  $k$ -cones exhibiting distinct topologies. b) Smith curves of three typical  $k$ -cones on the  $(k_x, ik_y)$  plane exhibiting distinct topologies. c) PB phases of the abnormal modes at four incident angles for the slab case. Dashed lines separate the whole space to two sub-regions (I and II). 3  $\times$ : Data are magnified by 3 times. d)  $\tilde{L}_{in,ex}/\tilde{L}_{tot}$  of the abnormally transmitted beam, obtained by the full theory (solid lines) and the lowest-order approximation (spheres). Inset: Approximated PB phase distribution at  $\theta_K^i = 0.5^\circ$ . e) A phase diagram with the  $\theta_c^i - w_0$  line separating the whole space to two subregions with distinct OAM properties.

EOAM in the abnormal mode, with their relative strengths varying with  $\theta_K^i$ .

The established picture helps us to identify an important parameter to control such a phase transition. Figure 4e shows that the critical angle  $\theta_c^i$  of the phase transition, defined as the angle where  $\tilde{L}_{in}/\tilde{L}_{tot} = 0.1$ , is a decreasing function of the beam width  $w_0$ . The physics is very clear: Increasing  $w_0$  effectively decreases the cut-off values of  $k^i$  in the incident beam, which diminishes the vortex contribution of region I, finally leading to the decrement of  $\theta_c^i$ .

## 4. Discussion and Extensions

### 4.1. Reinterpreting Results Computed by Previous Theories

We now reconcile the apparently different results on spin-Hall shifts yielded by our theory and the previous one,<sup>[16–18]</sup> as shown in Figure 2. Since our theory assumes a CP incidence, the transmitted beam with respect to an LP incidence actually contains four components—the normal and abnormal modes corresponds to different CP incidence (see Figure 5a). Therefore, the spin-polarized transmitted beam studied by previous theory is actually a linear combination of the normal and abnormal modes corresponding to incident beams with opposite spins. This pro-

cess can be schematically illustrated in Figure 5a and qualitatively expressed as

$$\begin{aligned} E_+^i(x^i, y^i) |+\rangle + E_-^i(x^i, y^i) |-\rangle &\rightarrow E_{++}^t(x^t, y^t + \Delta\gamma_{nor}) |+\rangle \\ &+ E_{+-}^t(x^t, y^t + \Delta\gamma_{abn}) |+\rangle + E_{-+}^t(x^t, y^t - \Delta\gamma_{abn}) |-\rangle \\ &+ E_{--}^t(x^t, y^t - \Delta\gamma_{nor}) |-\rangle \\ &= E_+^t(x^t, y^t - \Delta\tilde{\gamma}_+) |+\rangle + E_-^t(x^t, y^t - \Delta\tilde{\gamma}_-) |-\rangle \end{aligned} \quad (14)$$

Based on this picture, we find the spin-Hall shift  $\Delta\tilde{\gamma}_\pm$  under LP incidence (e.g., with initial condition  $E_+^i = E_-^i$ ) can be reinterpreted as a weighted combination of our spin-Hall shifts (see Section S5, Supporting information for detailed derivation)

$$\Delta\tilde{\gamma}_\pm \approx \pm \text{Re} \left\{ [t_{++}(\mathbf{K}^i)\Delta\gamma_{nor} + t_{+-}(\mathbf{K}^i)\Delta\gamma_{abn}] / [t_{++}(\mathbf{K}^i) + t_{+-}(\mathbf{K}^i)] \right\} \quad (15)$$

Calculated results with our theory are in excellent agreement with the existing ones<sup>[16–18]</sup> (Figure 5b). In particular, we find

$$\Delta\tilde{\gamma}_\pm \approx \pm \Delta\gamma_{abn} \text{Re}[t_{+-}(\mathbf{K}^i)/t_{++}(\mathbf{K}^i)] \quad (16)$$

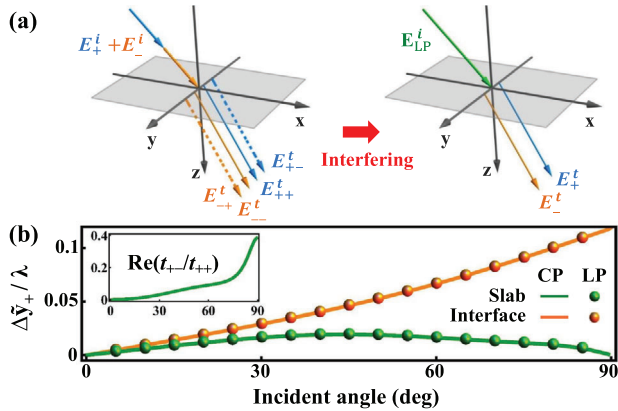


**Figure 5.** Reinterpreting the existing results with our theories. a) Schematics of using the CP-incidence results to reinterpret previous spin-Hall shifts under LP incidence. This process is also expressed by Equation (14). b) Spin-Hall shift  $\Delta\tilde{y}_+$  under LP incidence, obtained by reinterpretations with our CP-based theory (solid lines) and direct calculations using previous LP-based theory (spheres), in both single-interface and slab cases. Inset:  $\text{Re}[t_{+-}(K^i)/t_{++}(K^i)]$  as a function of incident angle for the slab case.

in the slab case since  $\Delta y_{\text{nor}} \equiv 0$  and  $|t_{++}| \gg |t_{+-}|$ . Such a formula well explains the intriguing  $\theta_K^i$ -dependence of  $\Delta\tilde{y}_+$  compared to  $\Delta y_{\text{abn}}$  (Figure 2c), because  $\text{Re}[t_{+-}(K^i)/t_{++}(K^i)]$  behaves differently as  $\Delta y_{\text{abn}}$  (inset to Figure 5b) and the competition between these two terms yields the final  $\Delta\tilde{y}_+ \sim \theta_K^i$  relation.

Our reinterpretations suggest that previous spin-Hall shifts obtained with LP incidences might not be fundamental quantities, and re-examining them under the CP bases could yield new insights, especially in the cases where Fresnel's coefficients exhibit singular behaviors.<sup>[27–32]</sup> For example, the spin-Hall shifts of reflected beam at incidence near Brewster angle is abnormally enhanced under LP incidences, while its mechanism remains obscure.<sup>[27–29]</sup> Employing our analyses using CP bases, we find that the reflected light beam exhibits a severely deformed pattern caused by the destructive interference between normal and abnormal modes, because of  $r_{+-}(K^i) = -r_{++}(K^i)$  at the Brewster angle. As the result, the centroid shift of the reflected beam is then anomalously increased.

#### 4.2. Experimentally Demonstrating the Topology-Induced Phase Transition with a $\epsilon_z \rightarrow 0$ Metamaterial Exhibiting Much Enhanced Efficiency

Since only the abnormal mode exhibits the topology-induced phase transition, to observe such effect more clearly in experiments, naturally one needs to enhance the generation efficiency of abnormal mode as large as possible. Such a generation efficiency is expressed as

$$\eta = P_z^t / P_z^i \approx |t_{+-}(K^i)|^2 = |t_{\text{TM}}(K^i) - t_{\text{TE}}(K^i)|^2 / 4 \quad (17)$$

where  $P_z^a = \int_{-\infty}^{\infty} \hat{z}^a \cdot \text{Re}(\mathbf{E}^* \times \mathbf{H}) d\mathbf{k}^a$  are the powers carried by the abnormal mode and the incident one. Equation (17) indicates that, to get an  $\eta$  value as large as possible, the interface should exhibit the following two features: i) it is optically transparent for incident light with different polarizations under certain incident angles and ii) two transmission coefficients are nearly out

of phase. Unfortunately, these two requirements are conflicting with each other at interfaces between air and isotropic dielectrics (with permittivity  $\epsilon$ ), since enlarging  $\epsilon$  can enhance the response difference but diminish the transmittance simultaneously. As a result, the maximum efficiency achieved by a normal material interface (e.g., a thin isotropic slab with  $\epsilon = 2.25$ ) is only in the order of  $10^{-5}$ .

The conversion efficiency can be significantly enhanced on a carefully designed metamaterial.<sup>[33,34]</sup> The key idea is to tune the anisotropic responses of the metamaterial along perpendicular ( $z$ ) and in-plane ( $xy$ ) directions, so as to largely enhance the difference in optical responses for two polarizations. Inspired by this argument, we designed a metamaterial slab (see Figure 6a for the picture of fabricated sample) with hollow-carved unit cell depicted in Figure 6b, which consists of four H-shaped metallic resonators embedded inside four dielectric side walls. A single H-shaped resonator supports two electric resonances for excitation fields polarized along  $z$  and  $x$  (or  $y$ ) directions, while arranging them in this way can ensure the whole system to exhibit identical responses in the  $xy$ -plane. Therefore, adjusting the geometric parameters of these metallic resonators to change their resonance frequencies, we finally design and fabricate a metamaterial with desired dielectric responses (i.e.,  $\epsilon_x = \epsilon_y$  and  $\epsilon_z$ ), and in turn, the desired optical responses at oblique incidences.

Figure 6c,d depict the experimentally measured transmission spectra of the fabricated metamaterial slab at different incident angles ( $\beta$ ), for waves taking TE and TM polarizations, respectively. Clearly, within the frequency range of interests (34–36 GHz), TE-polarized waves can pass through the slab with nearly 100% efficiency, insensitive to the incident angle  $\beta$ . In contrast, we find that the transmission spectra of TM-polarized waves at oblique incidences exhibit clear dips around a frequency  $f_m = 34.4$  GHz, exhibiting distinct behaviors as their TE counterparts. To reveal the underlying physics, we retrieve the effective-medium parameters of the designed/fabricated metamaterial from the transmission spectra obtained with finite-element-method simulations. We find that  $\epsilon_x = \epsilon_y = 1.2 - 68^2 / (f^2 - 45^2 + i0.159f)$  and  $\epsilon_z = 1.2 - 15.1^2 / (f^2 - 31.48^2 + i0.398f)$  with  $f$  denoting frequency in unit of GHz. For the TM polarization, we get  $\epsilon_z = 0.021 + i0.084i$  at the frequency  $f_m$ , which is near zero and responsible for blocking the TM-polarized wave which can “see” this dielectric response. On the other hand, we have  $\epsilon_x = \epsilon_y = 6.694 + i0.036$  and design the metamaterial thickness  $h = 1.61$  mm to enable a Fabry–Perot transmission peak around the working frequency  $f_m$ , which also explains that the transmission amplitude for TE-wave almost keeps around unity in the range of incident angles of interest (since Fabry–Perot resonance is not very sensitive to the incident angle). Putting these results into Equation (17), we immediately see that generation efficiency ( $\eta$ ) can be maximized at frequencies around  $f_m$  where two polarizations exhibit the largest anisotropic responses.

We now put the transmission coefficients  $\{t_{\text{TM}}(K^i), t_{\text{TE}}(K^i)\}$  (Figure 6e) into Equation (1) to numerically reconstruct the transmitted light beam. Insets to Figure 6f depicts the computed field patterns of the normal and abnormal light beams, at a reference plane  $10\lambda$  below the slab. The expected topology-induced phase transition is clearly shown in the evolutions of abnormal mode. Moreover,  $\eta$  of such effect realized at our metamaterial slab reaches up to 5% (blue spheres in Figure 6f) as the

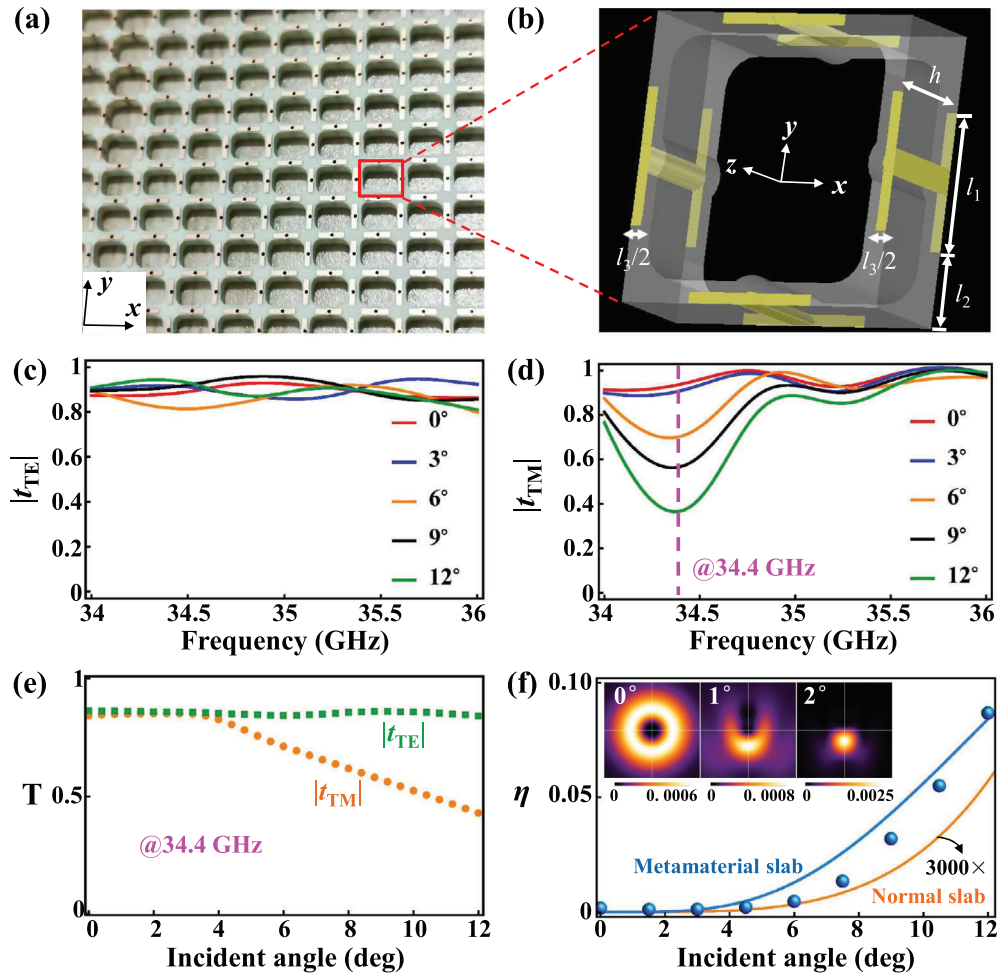


**Figure 6.** Experimental verification of the topological-induced phase transition with a realistic metamaterial slab. a) Sample photo. b) A unit cell of the metamaterial sample with thickness  $h = 1.61$  mm. Yellow: copper pieces with thickness being  $0.015$  mm and its conductivity being  $5.8 \times 10^7$  S  $m^{-1}$ ; Gray: substrate with its permittivity being  $3.66+0.0113i$ . The radius of the cylinder connecting the two arms of “H” is  $0.15$  mm. Other parameters:  $l_1 = 2.075$  mm,  $l_2 = 0.7125$  mm,  $l_3 = 0.4$  mm, and the side length of the unit cell is  $3.5$  mm (i.e.,  $l_1+2l_2$ ). c, d) Experimental measured transmission coefficients of the metamaterial slab at 34–36 GHz range. e) Measured transmission coefficients at 34.4 GHz frequency versus incident angle. f) Conversion efficiency calculated from the experimental transmission coefficients (blue spheres and solid lines respectively represents the direct experimental efficiency and calculated one from the retrieved effective permittivity) and a normal isotropic slab (orange line,  $\epsilon = 2.25$ ) with thickness  $h = 0.185 \lambda$  and beam waist  $w_0 = 15 \lambda$ . Insets: computed intensity patterns of the abnormal mode for three angles, whose intensities have been normalized to the maximum values of the respective normal modes.

incident angle is larger than  $10^\circ$ , exhibiting several thousand times enhancements compared to that at an isotropic dielectric slab ( $\epsilon = 2.25$ ). Analytical results (blue solid line) based on the retrieved effective-medium parameters of the metamaterial are in excellent agreement with experimental results on realistic structures, and further reveal the underlying physics of the discovered effect.

## 5. Conclusions

We have discovered a topology-induced phase transition in beam scatterings at sharp optical interfaces. The OAM properties of the abnormally scattered beams are dictated by Pancharatnam–Berry phases gained by every wave components inside the beam, which, depending on their relative angles with the central wave, can either contribute to vortex generation or spin-Hall shift, ul-

timately dictated by their topological natures. Varying the incident angle of beam can change the relative portions of these two contributions, driving the system to undergo a phase transition from IOAM-dominated region to EOAM-dominated one. We finally designed/fabricated a realistic metamaterial slab and experimentally illustrated such an intriguing effect which exhibits efficiencies several thousand times enhanced as compared to that on an isotropic slab made of conventional materials.

Our findings provide a unified picture to understand two previously discovered effects on the same foot, and can be extended to study other SOI-induced effects in light (e.g., spin-controlled vortex generation<sup>[1,9–12]</sup> and spin-Hall momentum shift<sup>[35–39]</sup> in inhomogeneous anisotropic media) and other waves (e.g., vortex-bearing electron beams).<sup>[40,41]</sup> More importantly, as the SOI of light plays an increasingly important role in nanophotonics,<sup>[42–48]</sup> plasmonics,<sup>[49–51]</sup> and topological photonics,<sup>[52–55]</sup> our results

may pave the way for a variety of applications, such as precision metrology,<sup>[56,57]</sup> edge detection,<sup>[58,59]</sup> particle manipulation,<sup>[60,61]</sup> and various spin-photon components.<sup>[42–45,62,63]</sup>

## Supporting Information

Supporting Information is available from the Wiley Online Library or from the author.

## Acknowledgements

X.L. and F.G. contributed equally to this work. X.L. would like to thank Zhong Hu and Yan Chen in Shanghai University for their help in experiments. This work was supported by the Natural Science Foundation of China (Grant Nos. 11734007, 11604087, 11674068, 11874142, and 11704240), the National Key Research and Development Program of China (Grant No. 2017YFA0303504), the Natural Science Foundation of Hunan Province (Grant No. 2018JJ1001), and Shanghai Science and Technology Committee (Grant No. 20JC1414602).

## Conflict of Interest

The authors declare no conflict of interest.

## Data Availability Statement

Data sharing is not applicable to this article as no new data were created or analyzed in this study.

## Keywords

berry phase, orbital angular momentum, phase transition, photonic spin-Hall effect, spin-orbit interaction of light, vortex

Received: November 7, 2020

Revised: March 23, 2021

Published online:

- [1] K. Y. Bliokh, F. J. Rodriguez-Fortuno, F. Nori, A. V. Zayats, *Nat. Photonics* **2015**, *9*, 796.
- [2] A. Aiello, P. Banzer, M. Neugebauer, G. Leuchs, *Nat. Photonics* **2015**, *9*, 789.
- [3] K. Y. Bliokh, F. Nori, *Phys. Rep.* **2015**, *592*, 1.
- [4] A. T. O'Neil, I. MacVicar, L. Allen, M. J. Padgett, *Phys. Rev. Lett.* **2002**, *88*, 053601.
- [5] J. Sinova, S. O. Valenzuela, J. Wunderlich, C. H. Back, T. Jungwirth, *Rev. Mod. Phys.* **2015**, *87*, 1213.
- [6] V. S. Liberman, B. Y. Zel'dovich, *Phys. Rev. A* **1992**, *46*, 5199.
- [7] K. Y. Bliokh, Y. P. Bliokh, *Phys. Lett. A* **2004**, *333*, 181.
- [8] K. Y. Bliokh, A. Niv, V. Kleiner, E. Hasman, *Nat. Photonics* **2008**, *2*, 748.
- [9] Z. Bomzon, V. Kleiner, E. Hasman, *Opt. Lett.* **2001**, *26*, 1424.
- [10] G. Biener, A. Niv, V. Kleiner, E. Hasman, *Opt. Lett.* **2002**, *27*, 1875.
- [11] L. Marrucci, C. Manzo, D. Paparo, *Phys. Rev. Lett.* **2006**, *96*, 163905.
- [12] R. C. Devlin, A. Ambrosio, N. A. Rubin, J. P. B. Mueller, F. Capasso, *Science* **2017**, *358*, 896.
- [13] S. Pancharatnam, *Proc. - Indian Acad. Sci., Sect. A* **1956**, *44*, 247.
- [14] M. V. Berry, *J. Mod. Opt.* **1987**, *34*, 1401.
- [15] M. Onoda, S. Murakami, N. Nagaosa, *Phys. Rev. Lett.* **2004**, *93*, 083901.
- [16] K. Y. Bliokh, Y. P. Bliokh, *Phys. Rev. Lett.* **2006**, *97*, 043901.
- [17] K. Y. Bliokh, Y. P. Bliokh, *Phys. Rev. E* **2007**, *75*, 066609.
- [18] O. Hosten, P. Kwiat, *Science* **2008**, *319*, 787.
- [19] Y. Qin, Y. Li, H. He, Q. Gong, *Opt. Lett.* **2009**, *34*, 2551.
- [20] M. Yavorsky, E. Brasselet, *Opt. Lett.* **2012**, *37*, 3810.
- [21] A. Ciattoni, A. Marini, C. Rizza, *Phys. Rev. Lett.* **2017**, *118*, 104301.
- [22] X. Ling, H. Luo, F. Guan, X. Zhou, H. Luo, L. Zhou, *Opt. Express* **2020**, *28*, 27258.
- [23] M. Born, E. Wolf, *Principles of Optics*, Cambridge University Press, Cambridge **1999**.
- [24] M. V. Berry, *Proc. R. Soc. A* **1984**, *392*, 45.
- [25] K. Y. Bliokh, M. A. Alonso, M. R. Dennis, *Rep. Prog. Phys.* **2019**, *82*, 122401.
- [26] A. Bekshaev, K. Y. Bliokh, M. Soskin, *J. Opt. A* **2011**, *13*, 053001.
- [27] H. Luo, X. Zhou, W. Shu, S. Wen, D. Fan, *Phys. Rev. A* **2011**, *84*, 043806.
- [28] L. Kong, X. Wang, S. Li, Y. Li, J. Chen, B. Gu, H. Wang, *Appl. Phys. Lett.* **2012**, *100*, 071109.
- [29] J. Ren, B. Wang, M. Pan, Y. Xiao, Q. Gong, Y. Li, *Phys. Rev. A* **2015**, *92*, 013839.
- [30] M. Kim, D. Lee, T. H. Kim, Y. Yang, H. J. Park, J. Rho, *ACS Photonics* **2019**, *6*, 2530.
- [31] H. Dai, L. Yuau, C. Yin, Z. Cao, X. Chen, *Phys. Rev. Lett.* **2020**, *124*, 053902.
- [32] M. Kim, D. Lee, H. Cho, B. Min, J. Rho, *Laser Photonics Rev.* **2021**, *15*, 2000393.
- [33] D. R. Smith, J. B. Pendry, M. C. K. Wiltshire, *Science* **2004**, *305*, 788.
- [34] N. Yu, F. Capasso, *Nat. Mater.* **2014**, *13*, 139.
- [35] N. Shitrit, I. Yulevich, E. Maguid, D. Ozeri, D. Veksler, V. Kleiner, E. Hasman, *Science* **2013**, *340*, 724.
- [36] L. Huang, X. Chen, B. Bai, Q. Tan, G. Jin, T. Zentgraf, S. Zhang, *Light: Sci. Appl.* **2013**, *2*, e70.
- [37] X. Ling, X. Zhou, X. Yi, W. Shu, Y. Liu, S. Chen, H. Luo, S. Wen, D. Fan, *Light: Sci. Appl.* **2015**, *4*, e290.
- [38] X. Luo, M. Pu, X. Li, X. Ma, *Light: Sci. Appl.* **2017**, *6*, e16276.
- [39] W. Luo, S. Sun, H. Xu, Q. He, L. Zhou, *Phys. Rev. Appl.* **2017**, *7*, 044033.
- [40] J. Harris, V. Grillo, E. Mafakheri, G. C. Gazzadi, S. Frabboni, R. W. Boyd, E. Karimi, *Nat. Phys.* **2015**, *11*, 629.
- [41] K. Y. Bliokh, I. P. Ivanov, G. Guzzinati, L. Clark, R. Van Boxem, A. B  ch  , R. Juchtmans, M. A. Alonso, P. Schattschneider, F. Nori, J. Verbeeck, *Phys. Rep.* **2017**, *690*, 1.
- [42] X. Yin, Z. Ye, J. Rho, Y. Wang, X. Zhang, *Science* **2013**, *339*, 1405.
- [43] J. Petersen, J. Volz, A. Rauschenbeutel, *Science* **2014**, *346*, 67.
- [44] D. O'Connor, P. Ginzburg, F. J. Rodr  guez-Fortu  o, G. A. Wurtz, A. V. Zayats, *Nat. Commun.* **2014**, *5*, 5327.
- [45] D. Pan, H. Wei, L. Gao, H. Xu, *Phys. Rev. Lett.* **2016**, *117*, 166803.
- [46] Z. Shao, J. Zhu, Y. Chen, Y. Zhang, S. Yu, *Nat. Commun.* **2018**, *9*, 926.
- [47] G. Hu, X. Hong, K. Wang, J. Wu, H. Xu, W. Zhao, W. Liu, S. Zhang, F. Garcia-Vidal, B. Wang, P. Lu, C. W. Qiu, *Nat. Photonics* **2019**, *13*, 467.
- [48] L. Sun, B. Bai, J. Wang, M. Zhang, X. Zhang, X. Song, L. Huang, *Adv. Funct. Mater.* **2019**, *29*, 1902286.
- [49] A. Pham, A. Zhao, Q. Jiang, J. Bellessa, A. Drezet, *ACS Photonics* **2018**, *5*, 1108.
- [50] M. Thomaschewski, Y. Yang, C. Wolff, A. S. Roberts, S. I. Bozhevolnyi, *Nano Lett.* **2019**, *19*, 1166.
- [51] Q. Xu, S. Ma, C. Hu, Y. Xu, C. Ouyang, X. Zhang, Y. Li, W. Zhang, Z. Tian, J. Gu, X. Zhang, S. Zhang, J. Han, W. Zhang, *Adv. Opt. Mater.* **2019**, *7*, 1900713.
- [52] Q. Guo, W. Gao, J. Chen, Y. Liu, S. Zhang, *Phys. Rev. Lett.* **2015**, *115*, 067402.

- [53] A. P. Slobozhanyuk, I. S. Sinev, A. K. Samusev, Y. F. Yu, A. I. Kuznetsov, A. E. Miroshnichenko, Y. S. Kivshar, *Laser Photonics Rev.* **2016**, *10*, 656.
- [54] W. J. M. Kort-Kamp, *Phys. Rev. Lett.* **2017**, *119*, 147401.
- [55] X. Liu, S. Xia, E. Jajtić, D. Song, D. Li, L. Tang, D. Leykam, J. Xu, H. Buljan, Z. Chen, *Nat. Commun.* **2020**, *11*, 1586.
- [56] X. Zhou, X. Ling, H. Luo, S. Wen, *Appl. Phys. Lett.* **2012**, *101*, 251602.
- [57] R. Wang, J. Zhou, K. Zeng, S. Chen, X. Ling, W. Shu, H. Luo, S. Wen, *APL Photonics* **2020**, *5*, 016105.
- [58] T. Zhu, Y. Lou, Y. Zhou, J. Zhang, J. Huang, Y. Li, H. Luo, S. Wen, S. Zhu, Q. Gong, M. Qiu, Z. Ruan, *Phys. Rev. Appl.* **2019**, *11*, 034043.
- [59] J. Zhou, H. Qian, C. Chen, J. Zhao, G. Li, Q. Wu, H. Luo, S. Wen, Z. Liu, *Proc. Natl. Acad. Sci. USA* **2019**, *116*, 11137.
- [60] S. Fu, C. Guo, G. Liu, Y. Li, H. Yin, Z. Li, Z. Chen, *Phys. Rev. Lett.* **2019**, *123*, 243904.
- [61] K. Dholakia, T. Cizmar, *Nat. Photonics* **2011**, *5*, 335.
- [62] L. Du, Z. Xie, G. Si, A. Yang, C. Li, J. Lin, G. Li, H. Wang, X. Yuan, *ACS Photonics* **2019**, *6*, 1840.
- [63] R. Jin, L. Tang, J. Li, J. Wang, Z. G. Dong, *ACS Photonics* **2020**, *7*, 512.